Celest Mech Dyn Astr (2015) 123:279–303
DOI 10.1007/s10569-015-9635-2

ORIGINAL ARTICLE

Stability of two groups of multi-revolution elliptic halo orbits in the elliptic restricted three-body problem

Hao Peng[1] · **Shijie Xu**[1]

Received: 27 April 2014 / Revised: 23 May 2015 / Accepted: 30 June 2015 /
Published online: 23 July 2015

Abstract The multi-revolution elliptic halo (ME-Halo) orbit is a kind of strictly periodic orbit existing in the elliptic restricted three-body problem (ERTBP) model. Its remarkable features include that it survives the eccentricity perturbation of the primaries, it has a long period commeasurable with the primary period and that its stability property varies greatly as the eccentricity. The authors utilized continuation methods together with the multi-segment optimization method to generate two groups of ME-Halo orbits, and then systematically investigated their stability evolution with respect to the eccentricity and the mass ratio of the primaries. These parameters show complicate impacts on the stability. Some ME-Halo orbits can possess more than one pairs of real eigenvalue, some have negative real eigenvalues or complex eigenvalues out of the unit circle. For certain parameters, continuation failures are observed to be accompanied by a series of eigenvalue collision and bifurcations. The results in this paper can help to understand the nonautonomous dynamic of the ERTBP and can further aid in understanding the dynamical environment for real-world applications and, thus, contribute to the trajectory development process.

Keywords Elliptic restricted three-body problem (ERTBP) · Strictly periodic orbit · Continuation method · Stability · ME-Halo orbit

1 Introduction

Since Euler first found three collinear libration points of Circular Restricted Three-Body Problem (CRTBP) in 1767 and Lagrange found the other two triangular libration points in 1772 (Meyer et al. 2009), many mysteries in this fascinating field have been revealed and fruitful applications in space exploration have been yielded. In 1967 Szebehely comprehen-

✉ Hao Peng
AstroH.Peng@gmail.com

Shijie Xu
starsjxu@163.com

[1] Beihang University, Beijing, China

sively surveyed both analytical and numerical outcomes until his time (Szebehely 1967). Farquhar and Kamel then revealed the existence of halo orbit and proposed to use it as a relay to communicate with the far side of the Moon (Farquhar and Kamel 1973). Later Richardson constructed the third-order analytical solution of halo orbits using Lindstedt–Poincaré method in the truncated system (Richardson 1980), with which the shooting method was applied to generate halo orbits in the full CRTBP. Howell and Pernicka improved it and developed the multiple shooting method to compute halo and Lissajous orbits in more realistic systems (Howell and Pernicka 1987). The research in the CRTBP provides new possibilities in practical applications. Belbruno studied temporary captures by the primary in the CRTBP and proposed the weak stable region (WSB) theory, which was once utilized to rescue Hiten by designing a low-energy transfer to the Moon (Belbruno et al. 2012). More recently, Barden, Howell, Lo, Koon, Gomez and other researchers introduced the dynamical system theory to CRTBP (Barden et al. 1996; Koon et al. 2000; Gomez et al. 2004; Koon et al. 2011), which is a relatively modern technique. They developed theories of libration point orbits and the associated invariant manifolds, and designed low-energy transfer orbits by Poincaré sections.

The motion of planets in the Solar System can be better described by Keplerian elliptic orbits with eccentricity e ranging from 0.0086 to 0.2488 (Russell 2012), and Parker and Anderson (2014) also claimed that the most notable perturbation leading the orbit to diverge from being periodic was the nonzero eccentricity of the orbits of the primaries. As a consequence, research priorities were partially turned to extending the results of the CRTBP to the elliptic restricted three-body problem (ERTBP). The next step was naturally to focus on the existence and stability of the libration periodic orbits in the ERTBP. Heppenheimer studied the out-of-plane motion in the ERTBP utilizing Jacobi elliptic functions (Heppenheimer 1973). He constructed linear solution of the out-of-plane motion and used Lindstedt–Poincaré method to obtain a third order expansion. He claimed that the eccentricity tended to decrease the period while the nonlinearity tended to increase the period. So one can expect the period of in-plane, out-of-plane and the primary to be commensurable pairwise. Recently Hou and Liu constructed analytical expansion of collinear libration point orbits in the ERTBP by Lindstedt–Poincaré method (Hou and Liu 2011). The result is complicated since the appearance of eccentricity requires the expansion with one more parameter. Broucke had first systematically studied the stability of periodic orbits in the planar ERTBP (Broucke 1969). Three important properties of the planar ERTBP, which are also true in spatial case, are given as: the absence of Jacobi integral; discrete periodic orbits and two system parameters, the mass ratio μ and the eccentricity e. But the study was limited to the planar situation and period orbits were mostly constructed in systems with $\mu > 0.2$, which makes them less meaningful for solar planetary system. Sarris continued a vertical Lyapunov orbit with period 2π in the CRTBP to ERTBP along both μ and e, then he studied their stability and divided the stability coefficients space into 12 regions (Sarris 1989). But the system he investigated is also with a large μ which leads to periodic orbits with large periods. His one important state is that the ERTBP model cannot have both axial and bilateral symmetry at the same time. Gurfil and Kasdin applied niching genetic algorithm to search practically stable geocentric orbits in the ERTBP and discussed their applications (Gurfil and Kasdin 2002). These orbits remain finite motion for a long time but they revolve around the primary rather than libration points. Gurfil and Meltzer worked out an analytical approximation of the monodromy matrix of orbits in linearized ERTBP (Gurfil and Meltzer 2007), which is very helpful in stationkeeping problem but the study of the stability requests full model monodromy matrix. Antoniadou and Voyatzis had investigated resonant periodic orbits in the general three-body problem by continuation starting with periodic orbits in the ERTBP (Antoniadou and Voyatzis 2013).

Practical applications of ERTBP are also drawing great attentions, so periodic orbits with interesting properties different from that in the CRTBP are needed to be explored, which is as well the aim of this paper. Hiday and Howell had studied the optimal transfer between libration point orbits in the ERTBP since 1992 (Hiday and Howell 1994). Multiple shooting method could also be used to construct Lissajous orbits in the ERTBP (Howell and Pernicka 1987; Pernicka 1990). Using the same method, Mahajan and Pernicka recently investigated the construction of halo like orbits in asteroidal ERTBP and proposed their applications (Mahajan and Pernicka 2012). Later, Mahajan presented more results around several asteroids and as well worked out an orbit control strategy (Mahajan 2013). But the periodic orbit they investigated is not strictly periodic but only close after several revolutions, and the stability of these orbit is investigated by the monodromy matrix of only one revolution of the orbit, which actually only reflects local stability properties. For more accurate studies, Campagnola generated elliptic halo orbit possessing periods commensurable with that of the primaries, and found the stability bifurcation of these orbit (Campagnola et al. 2008). He also designed the gravitational capture of BepiColombo mission and found that the resulted trajectory shadowed the manifold of a halo like orbit in the Sun–Mercury ERTBP (Campagnola 2010). Qi et al. studied the gravitational capture in the Sun–Mercury ERTBP (Qi et al. 2014b) and Earth–Moon ERTBP (Qi and Xu 2014). It should be noticed that Qi et al. (2014a) also investigated the problem in a four-body problem model, which is a more accurate approximation of the Sun–Earth–Moon system. From another perspective, Hyeraci and Topputo numerically investigated the role of true anomaly in ballistic capture as an extension of the WSB theory, and proposed a method to help design missions in planar ERTBP (Hyeraci and Topputo 2010, 2013). In the opinion of the authors, no enough attention has been paid on the studies of the strictly periodic orbits in the ERTBP.

In this paper, the authors present a systematic study of the stability of two groups of multi-revolution elliptic halo (ME-Halo) orbits in the ERTBP. The ME-Halo orbit is strictly periodic and has a long period, which is rationally commeasurable with that of the primary bodies. The results in this contribution can serve as a fresh supplement to the study of the ERTBP. The observation of the stability evolutions of the ME-Halo can help in understanding the nonautonomous dynamics of the ERTBP. The eigenvalues of the group of ME-Halo orbit in this paper shows various collision and bifurcations, as a consequence of the appearance of the eccentricity. Their special features orbit can also provide new choices of nominal orbits in space mission design.

The paper is organized as following. In the second section, the generation and classification of ME-Halo orbits are elaborated, where the multi-segment optimization method is used to continue ME-Halo along both μ and e. In the third section, numerical results about the two groups of orbits are demonstrated and discussed in detail. Collisions and bifurcations of eigenvalues of the monodromy matrix are also summarized. In the last section, conclusions and related speculations are presented.

2 Background

2.1 Dynamic models

The full three-body problem has no complete solution because there are 18 first order differential equations but only 10 general integrals (Meyer et al. 2009). For the application of space trajectory design, an intuitive approach is to study the restricted three-body problem

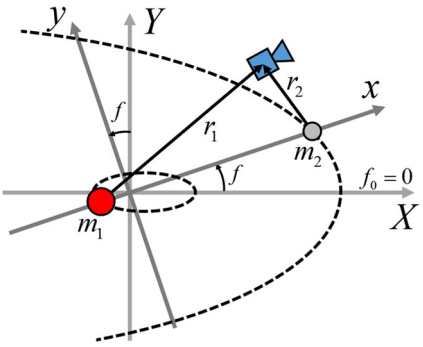

Fig. 1 Barycenter inertial coordinate frame (X, Y, Z) and barycenter synodic coordinate frame (x, y, z). The z-axis finishes the right handed system pointing out of the paper. In the CRTBP the primary orbit (*dashed arc*) is circular while in the ERTBP it is *elliptical*. In the ERTBP, the epoch when primaries are at periapsis is set to be $f_0 = 0$. The rotation angle of synodic frame if given by the true anomaly f

(RTBP), where the mass of the third body, usually a spacecraft, tends to zero and so that it does not affect the motion of the primaries. In the RTBP, the motion of this infinitesimal third body under the attraction of other two primaries' gravity fields is of interest. In this section a brief review of the equation of motion in the CRTBP and ERTBP is given.

In the CRTBP, the primaries revolves each other on Keplerian circular orbit around their common barycenter. Nechvile first employed a transform from the inertial coordinate frame to a synodic coordinate frame, with which equations of motion are most concise expressed and there comes the Jacobi integral. The origin of the synodic rotating coordinate frame locates at the barycenter. The x-axis points from the larger primary m_1 to the smaller one m_2. The z-axis is parallel with the angular momentum (pointing out of the paper) and the y-axis finishes the right-handed system. In Fig. 1 the eccentricity of the primary orbit (dashed arcs) is zero for the CRTPB model. The motion is normalized by adopting the distance between primaries r_{12} as the length unit, the total primary mass $(m_1 + m_2)$ as the mass unit, and the reciprocal of angular velocity n as the time unit, so that m_1 is fixed at $x_1 = -\mu$ and m_2 at $x_2 = 1 - \mu$, where the scaled mass of the smaller primary $\mu = m_2/(m_1 + m_2)$ is introduced as the only system parameter. In this way, the equations of motion for the CRTBP is given by (Szebehely 1967)

$$\begin{aligned} \ddot{x} - 2\dot{y} &= \Omega_x \\ \ddot{y} + 2\dot{x} &= \Omega_y \\ \ddot{z} &= \Omega_z \end{aligned} \tag{1}$$

where

$$\Omega(x, y, z) = \frac{1}{2}(x^2 + y^2) + \frac{1-\mu}{r_1} + \frac{\mu}{r_2} + \frac{1}{2}\mu(1-\mu) \tag{2}$$

with $r_1 = \sqrt{(x+\mu)^2 + y^2 + z^2}$ and $r_2 = \sqrt{(x-1+\mu)^2 + y^2 + z^2}$.

In the ERTBP, the primaries rotate each other on a Keplerian elliptic orbit (dashed ellipse in figure). The distance between primaries r_{12} is changing with true anomaly f, thus with time t, and is given by

$$r_{12}(f) = \frac{a_{12}(1-e^2)}{1 + e\cos f} \tag{3}$$

where a_{12} is the semimajor axis of primaries. A similar synodic coordinate frame is utilized, in which the system is instantaneously normalized by $r_{12}(f)$, the total primary mass $(m_1 + m_2)$ and the reciprocal of the mean motion $\bar{n}$. So the synodic frame is not only pulsating but also non-uniformly rotating now. Furthermore, the independent variable is transformed from time

t to true anomaly f by the chain rule

$$\frac{\mathrm{d}}{\mathrm{d}t} = \frac{\mathrm{d}f}{\mathrm{d}t} \cdot \frac{\mathrm{d}}{\mathrm{d}f} = \sqrt{\frac{G(m_1 + m_2)}{a^3(1-e^2)^3}}(1 + e\cos f)^2 \cdot \frac{\mathrm{d}}{\mathrm{d}f} \tag{4}$$

In this way equations of motion of the third body in the ERTBP is given in the pulsating synodic frame by (Szebehely 1967)

$$\begin{aligned} x'' - 2y' &= \omega_x \\ y'' + 2x' &= \omega_y \\ z'' &= \omega_z \end{aligned} \tag{5}$$

where

$$\omega(x, y, z, f) = (1 + e\cos f)^{-1}\tilde{\Omega}(x, y, z) \tag{6}$$

$$\tilde{\Omega}(x, y, z) = \Omega(x, y, z) - \frac{1}{2}e\cos f\, z^2 \tag{7}$$

Primes over coordinates indicate differentials with respect to true anomaly f. The same symbols (x, y, z) adopted for coordinate components will not cause confusion in the paper. The epoch when primaries are at their periapsis is set to be $f_0 = 0$ as illustrated in Fig. 1. Although Eqs. (1) and (5) show identical forms, ω differs from Ω greatly. The ERTBP explicitly depends on the independent variable f through $\omega(x, y, z, f)$ in Eq. (6), so it is a nonautonomous system. Besides, because of the trigonometric function introduced by Eqs. (4), (6) and (7), the ERTBP is also a periodic system with period 2π. Therefore, as a well-known fact, there does not exist the Jacobi integral in the ERTBP, which is used to reduce the system by one dimension in the CRTBP (Szebehely 1967; Broucke 1969).

2.2 Multi-revolution elliptic halo orbit

The periodic orbit is the only type of orbits that we can ever hope to understand completely throughout their evolution from the distant past to the distant future since the entire course of their evolution is determined by knowledge over a finite time interval, i.e. the period (Wiggins 2003). A fix point can be viewed as a periodic orbit with zero or infinite period. The most intensively investigated periodic orbits in the CRTBP include planar and vertical Lyapunov orbit families, prograde and retrograde orbit families around small primary, halo orbit families at collinear libration points $L_{1,2,3}$ and horseshoe-shape orbits around triangular libration points $L_{4,5}$. But in the ERTBP most of these orbits do not survive the perturbation caused by the eccentricity e of the primaries, because the system is non-autonomous and the libration point itself is osculating with primaries.

Following the way similar in the CRTBP (Szebehely 1967), libration points of the ERTBP in the pulsating synodic frame can be obtained. Letting the first and second order differential terms in Eq. (5) equal to zero, we have

$$\omega_x = \omega_y = \omega_z = 0 \tag{8}$$

The solution gives five fixed points in the pulsating synodic frame, which locates exactly at the same position with that in the CRTBP. However, they are only geometrical libration points but not dynamical ones anymore. Because the collinear points are oscillating along the x-axis with the pulsating frame, and the triangular points are oscillating to maintain the equilateral triangle with primaries as well. Nevertheless, the pulsating region is bounded, which should be referred to as *libration point region* more precisely. So a spacecraft can still

revolve around such regions, and in the synodic pulsating frame it appears on a libration point orbit similar to that in the CRTBP. But actually the orbit has stretched a lot along x-axis in a non-pulsating frame, as will be shown by several figures later.

General periodic solutions in the ERTBP are not easy to detect, but the symmetric periodic orbits is relatively easier. The ERTBP system (5) keeps invariance under the map (Sarris 1989)

$$(f; x, y, z, \dot{x}, \dot{y}, \dot{z}) \rightarrow (-f; x, -y, z, -\dot{x}, \dot{y}, -\dot{z}) \tag{9}$$

This relation indicates that the periodic orbit is symmetric with respect to x–z plane in the synodic frame. In fact Sarris also discussed other symmetries, but this one is adopted by the authors to generate the orbit investigated in this paper. According to it, Moulton first expressed (Moulton 1920), and Broucke later cited (Broucke 1969) the strong periodicity criterion for planar ERTBP as follows,

> For an orbit to be periodic it is sufficient that it has two perpendicular crossings with the syzygy-axis, and that the crossings happen at moments when the two primaries are at an apse, (i.e., at maximum or minimum elongation, or apoapsis and periapsis).

The extension of this criteria in the spatial situation has been known at least since 1980s by researchers such as Ichtiaroglou and Michalodimitrakis (Ichtiaroglou 1980; Ichtiaroglou and Michalodimitrakis 1980). Recently, Campagnola (2010) expressed the sufficient criterion in the spatial ERTBP as,

> For an orbit to be periodic in the ERTBP, it is sufficient that it has two perpendicular crossing with either the normal plane or the syzygy axis, or both of them, when the primaries are at apse.

According to the criterion, the period T_E of a symmetric periodic orbit in the ERTBP must be an integral multiple of the system period 2π. It is still difficult to construct a periodic orbit in the ERTBP with this criterion. Usually it is started from a periodic orbit with a particular period T_C in the CRTBP, and continue it into the ERTBP. So T_E must be an integral multiple of T_C as well. These two relationships can be expressed as the commeasurable constraint below,

$$T_E = N \cdot 2\pi = M \cdot T_C, \quad M, N \in \mathbb{N}^+, \tag{10}$$

where M indicates the revolution number of the third body around the libration region and N indicates the revolution of the primaries within one orbit period. So actually it is an $M : N$ resonant orbits in the ERTBP. It should be noticed that T_E and T_C are both given in true anomaly f, but in the CRTBP the true anomaly coincides with the scaled time so T_C is specified with time unit usually. Broucke had studied the planar Lyapunov orbit in the ERTPB where $M = 1$ (Broucke 1969), but the range of the period T_C of the halo orbit family in the CRTBP with a small μ is usually too narrow to have orbits with $M = 1$, as illustrated by the Earth–Moon system in Fig. 2. Therefore the continuation needs to start from a halo orbit with $M > 1$ revolutions. These periodic orbits will stay around the libration point region for a long time, which is N times of the primary period. Campagnola first generated these orbits in the Sun–Mercury and the Earth–Moon systems (Campagnola et al. 2008), where they were referred to as Elliptic Halo Orbits. Considering the orbits the authors have interest in close up after M revolutions, which are different from that in the ERTBP with a large μ, they are referred to as *ME-Halo* orbits hereinafter, with the emphasis on their multiple revolutions property, and the term *halo orbit* still means the traditional halo orbit in the CRTBP. This special properties can be helpful in observation missions or libration gate missions.

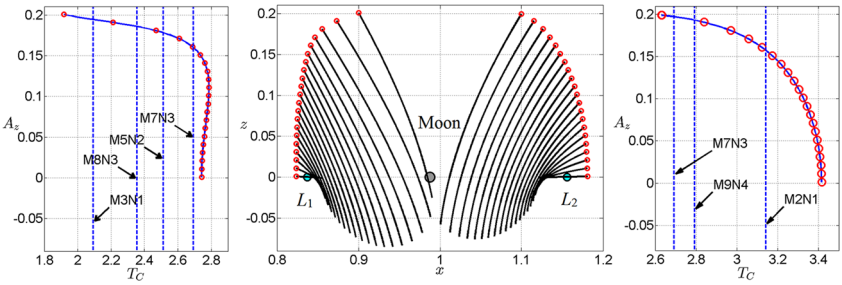

Fig. 2 Halo orbit families around L_1 and L_2 point in Earth–Moon system ($\mu = 0.0122$), and their period range. In the *center plot* the halos are illustrated on the x–z projections. The *left* (*right*) plot shows the z-axis amplitude A_z with respect to the period T_C of the L_1 (L_2) family. The *dashed vertical lines* show some periods satisfying the commeasurable constraint

The very first step of the continuation is to find a halo orbit with precise period T_C satisfying Eq. (9). Since there is no available analytical method so far as we know, such an orbit is numerically extracted from the whole halo orbit family by a dichotomy of A_z. Before this, a proper set of (M, N) should be specified. Take the Earth–Moon system as an example, Fig. 2 illustrates Halo orbit families around L_1 and L_2 point on the x–z plane (center plot) and curves of the z-axis amplitude A_z with respect to their period (left and right plots resp.). These orbits are generated by continuations along A_z with simple differential correction method as reviewed in the next subsection. Vertical dashed lines shows different sets of (M, N) as annotated in the figure, which satisfies Eq. (9). There are infinite sets of (M, N) close to any desired period since the rational number is dense. But it should be aware of that too large M and N will cause numerical difficulties for stability study as will be discussed later in Sect. 2.5, so in this paper $M = 5$ and $N = 2$ is chosen, which is abbreviated as $M5N2$ hereinafter. After having chosen the desired $T_C = 2N\pi/M$ for $e = 0$, the initial condition $\boldsymbol{X}_0(e = 0)$ of the corresponding halo orbit is extracted by dichotomies. Then the eccentricity e is increased gradually by the continuation step δe, and $\boldsymbol{X}_0(e + \delta e)$ is obtained by adjusting $\boldsymbol{X}_0(e)$ with the multi-segment optimization method as will be elaborated in next section. In this way, a group of orbits parameterized by the eccentricity e is obtained. In fact, a group of orbits parameterized by the mass ratio μ can be obtained as well by continuation along μ. The numerical methods used for continuation of both halo orbit and ME-Halo orbit are elaborated in the next subsection.

2.3 Multi-segment optimization method

The general procedure of generating a halo orbit is to use the third order analytical solution developed by Richardson (Richardson 1980) as an initial guess and then use the differential correction method to close it up (Howell and Pernicka 1987). In order to be self-consistent, a brief summary of this method is given first. Define the state of the third body in the CRTPB as $\boldsymbol{X}(t) = [x, y, z, \dot{x}, \dot{y}, \dot{z}]^{\mathrm{T}}$, so that Eq. (1) can be transformed into a group of six first-order differential equations. The halo orbit should leave and return to the x–z plane perpendicularly after half a period. The initial state vector is $\boldsymbol{X}(t_0) = \boldsymbol{X}_0 = [x_0, 0, z_0, 0, \dot{y}_0, 0]^{\mathrm{T}}$ and after a propagation of half a period $T/2$ it should be $\hat{\boldsymbol{X}}(T/2, \boldsymbol{X}_0) = \hat{\boldsymbol{X}}_{T/2} = [\hat{x}, 0, \hat{z}, 0, \hat{\dot{y}}, 0]^{\mathrm{T}}_{T/2}$. The error needed to be corrected after each iteration is given by $\delta\boldsymbol{X}_{T/2} = \hat{\boldsymbol{X}}_{T/2} - \boldsymbol{X}_{T/2}$. The initial condition $\boldsymbol{X}_0$ and period T is modified by a small correction $(\delta\boldsymbol{X}_0, \delta T)$ so that

$$0 = \hat{\boldsymbol{X}}_{T/2} - \boldsymbol{X}_{T/2} = \frac{\partial \boldsymbol{X}_{T/2}}{\partial \boldsymbol{X}_0}\delta\boldsymbol{X}_0 + \frac{\partial \boldsymbol{X}_{T/2}}{\partial T}\delta T + O\left(\|\delta\boldsymbol{X}_0\|^2\right) + O\left((\delta T)^2\right), \tag{11}$$

where $O(\cdot)$ represents higher order infinitesimals. Define $\boldsymbol{\Phi}(t, t_0) = \partial \boldsymbol{X}(t, \boldsymbol{X}_0)/\partial \boldsymbol{X}(t_0, \boldsymbol{X}_0)$ to be the state transition matrix (STM) from t_0 to $T/2$ of the orbit passing $\boldsymbol{X}_0$. So that $\partial \boldsymbol{X}_{T/2}/\partial \boldsymbol{X}_0 = \boldsymbol{\Phi}(T/2, t_0)$ in Eq. (11). It satisfies the first-order variation equation

$$\dot{\boldsymbol{\Phi}}(t, t_0) = \boldsymbol{A}_C(\boldsymbol{X}, t)\boldsymbol{\Phi}(t, t_0), \quad \boldsymbol{\Phi}(t_0, t_0) = \boldsymbol{I}_6, \tag{12}$$

where $\boldsymbol{A}_C(\boldsymbol{X}, t)$ is the Jacobian of Eq. (1)

$$\boldsymbol{A}_C(\boldsymbol{X}, t) = \begin{bmatrix} 0 & \boldsymbol{I}_3 \\ \boldsymbol{H}_C & \boldsymbol{K}_C \end{bmatrix}_{(\boldsymbol{X},t)}, \quad \boldsymbol{H}_C = \begin{bmatrix} \Omega_{xx} & \Omega_{xy} & \Omega_{xz} \\ \Omega_{yx} & \Omega_{yy} & \Omega_{yz} \\ \Omega_{zx} & \Omega_{zy} & \Omega_{zz} \end{bmatrix}_{(\boldsymbol{X},t)},$$
$$\boldsymbol{K}_C = \begin{bmatrix} 0 & 2 & 0 \\ -2 & 0 & 0 \\ 0 & 0 & 0 \end{bmatrix}_{(\boldsymbol{X},t)}. \tag{13}$$

The subscripts of Ω indicate partial differentials with respect to corresponding coordinates. Truncate Eq. (11) at the first order, extract only the adjustable terms and we have

$$\begin{bmatrix} \delta y \\ \delta \dot{x} \\ \delta \dot{z} \end{bmatrix}_{T/2} = \begin{bmatrix} \phi_{2,1} & \phi_{2,3} & \phi_{2,5} \\ \phi_{4,1} & \phi_{4,3} & \phi_{4,5} \\ \phi_{6,1} & \phi_{6,3} & \phi_{6,5} \end{bmatrix} \begin{bmatrix} \delta x_0 \\ \delta z_0 \\ \delta \dot{y}_0 \end{bmatrix} + \begin{bmatrix} \dot{y}_1 \\ \ddot{x}_1 \\ \ddot{z}_1 \end{bmatrix}_{T/2} \delta T/2, \tag{14}$$

where $\phi_{i,j}$ is the i-th row and the j-th column of $\boldsymbol{\Phi}(T/2, t_0)$. Furthermore, stop the propagation at $y_1 = 0$ so that $\delta y = 0$, then Eq. (14) can be simplified to be

$$\begin{bmatrix} \delta \dot{x}_1 \\ \delta \dot{z}_1 \end{bmatrix} = \begin{bmatrix} \phi_{4,1} & \phi_{4,3} & \phi_{4,5} \\ \phi_{6,1} & \phi_{6,3} & \phi_{6,5} \end{bmatrix} \begin{bmatrix} \delta x_0 \\ \delta z_0 \\ \delta \dot{y}_0 \end{bmatrix} - \frac{1}{\dot{y}_1} \begin{bmatrix} \ddot{x}_1 \\ \ddot{z}_1 \end{bmatrix} \begin{bmatrix} \phi_{2,1} & \phi_{2,3} & \phi_{2,5} \end{bmatrix} \begin{bmatrix} \delta x_0 \\ \delta z_0 \\ \delta \dot{y}_0 \end{bmatrix}. \tag{15}$$

In this paper the continuation is carried out along z-axis amplitude A_z, so δz_0 is fixed to be zero. Then the desired correction $\delta \boldsymbol{X}_0 = [\delta x_0, 0, 0, 0, \delta \dot{y}_0, 0]^{\mathrm{T}}$ can be solved from Eq. (15). The correction needs to be done iteratively until a required tolerance reached.

This method is adopted to generate all the halo orbit families in this study. But for ME-Halo orbits, it has some limitations. Its convergence domain is small for a nonlinear problem, hence it requires a good initial guess. And a long-time integration of nonlinear equations will almost certainly fail the method even a good initial guess is available. Sometimes it will converge to retrograde distant orbit around primaries because it does not control the boundary of the correction $(\delta \boldsymbol{X}_0, \delta T)$. Other alternative methods include the multiple (or two-level) differential correction method (Howell and Pernicka 1987), evolutionary optimization method (Tarragó 2007; Martin et al. 2010) and so on. An economical method, which means it is easier to code and switch between different solvers but at the same time keeps high efficiencies, is desired by us, so that more attention could be paid on other subjects, rather than realizing complex advanced algorithm. Moreover, considering that the differential correction method is essentially a simple Newton's method without linear step searching (in the view of optimization field), it would be helpful to re-describe the shooting problem as an optimization problem and solve it with mature solvers.

The initial state $\boldsymbol{X}(f_0) = \boldsymbol{X}_0$ of the ME-Halo orbit in the ERTBP and the state after integrated for half period $\boldsymbol{X}_{T/2}$ are

$$\boldsymbol{X}_0 = \boldsymbol{X}(f_0) = [x_0, 0, z_0, 0, y_0', 0]^{\mathrm{T}}, \tag{16}$$
$$\boldsymbol{X}_{T/2} = \boldsymbol{X}(f_0 + T_E/2) = [x, y, z, x', y', z']^{\mathrm{T}}_{f_0+T_E/2}, \tag{17}$$

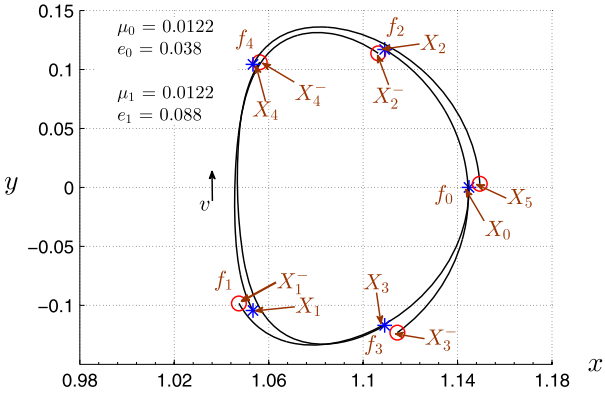

Fig. 3 Illustration of the multi-segments optimization method. The orbit is broken into several segments and continuous constraints are applied at connection points. Terminal constraints are applied to require the state $\boldsymbol{X}_5$ are perpendicular with the x–z plane

where the primes over coordinates indicate differentials with respect to true anomaly f. It is important to realize that in the ERTBP the independent variable at the same time indicates the phase angle of the primaries, so not only the duration $T_E/2$ but also the initial epoch f_0 must be specified, as given at the subscripts of Eq. (17). This is a nonautonomous feature of the ERTBP. According to the periodicity criteria of the ERTBP, $\boldsymbol{X}_{T/2}$ should be perpendicular to the x–z plane, i.e., at the half part of ME-Halo orbit there should be

$$y_{T_E/2} = x'_{T_E/2} = z'_{T_E/2} = 0. \tag{18}$$

Borrowing the idea of the multiple shooting method introduced by Howell and Pernicka to calculate Lissajous orbits (Howell and Pernicka 1987), the initial orbit is broken into n segments, as illustrated in Fig. 3. $\boldsymbol{X}_i$ and f_i $(i = 0, 1, \ldots, n-1)$ are the starting state and epoch of the $(i+1)$-th segment. Integrating $\boldsymbol{X}_i$ at from f_i to f_{i+1} gives $\boldsymbol{X}_{i+1}^-$, which is the end state of this segment. If the obtained orbit is smoothly connected, it should be identical to X_{i+1}, which can be expressed as

$$\boldsymbol{X}_{i+1}^-(\boldsymbol{X}_i, f_i) = \boldsymbol{X}_i, \quad i = 0, \ldots, n-2, \tag{19}$$

where X_{i+1}^- is formulated as a function of the previous state and epoch. These $6 \cdot (n-1)$ equations will serve as the nonlinear constraints in the optimization problem. In this way, $\boldsymbol{X}_{T/2}$ is the last integration end point $\boldsymbol{X}_n = [x_n, y_n, z_n, x'_n, y'_n, z'_n]^{\mathrm{T}}$ at $f_{T/2} = f_0 + T_E/2$, so it should satisfies Eq. (18), and other three components are free. Use this property to define the cost function of the optimization problem as

$$\min \ J(\boldsymbol{X}_0, f_0; \ldots; \boldsymbol{X}_i, f_i; \ldots; \boldsymbol{X}_{n-1}, f_{n-1}) = \sqrt{y_n^2 + x_n'^2 + z_n'^2}, \tag{20}$$

At last, the problem is well defined by Eq. (20) with differential constraints given by Eq. (5) and nonlinear constraints given by Eq. (19). The minimum of this problem should be zero and it implies a periodic orbit. If an initial orbit guess in the ERTBP with μ_0 and e_0 is given, changing e_0 (or μ_0) to e_1 (or μ_1) and solving the problem in the ERTBP with new parameters will finish one step of the continuation of the ME-Halo orbit. Since both the optimization form and the segmentation are the key ideas of this continuation process, it is referred to as the *Multi-segment Optimization Method* in this paper.

In this paper, interior point method embedded in Matlab function *fmincon* is adopted as the default solver. The tolerances for nonlinear constraints can be set differently for position and velocity components. It converges quickly and allows to use a rough initial guess, which is simply the previous ME-Halo orbit. Extrapolation techniques for initial guesses show some

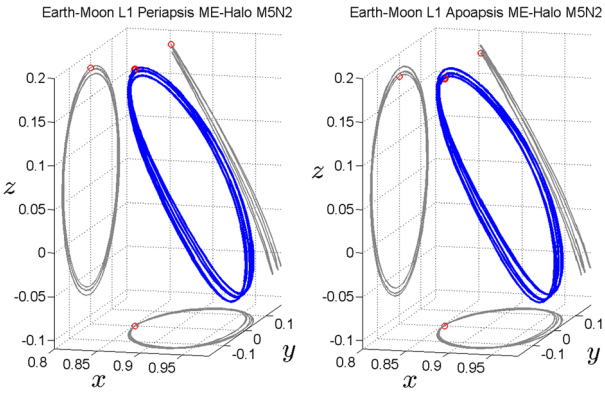

Fig. 4 Earth–Moon L_1 Periapsis (*left plot*) and Apoapsis (*right plot*) ME-Halo orbit with $M5N2$ in the pulsating synodic frame

improvements but not that much efficient, possible because the interior point solver is already adequately efficient. The Sequential Quadratic Programming (SQP) method in *fmincon* is also utilized in some studies, for example when trying to re-close up a continuation result with higher accuracy. The SQP appears faster than interior point method when a good initial guess is available. The convergence of the algorithm increases as n increases, but the time cost increases as well. So after a trial and error process, we recommend $M/2 \leq n \leq 2M$ for continuations along e and $n \geq 3M$ for continuations along μ.

2.4 Four groups of ME-Halo orbits

The halo orbit family exists continuously in the CRTBP with fixed μ and $e = 0$, and it is parameterized by the z-axis amplitude A_z. ME-Halo orbits with different sets of (M, N) exist discretely in the ERTBP with fixed set of (μ, e) because of the commeasurable constraint. However, for fixed (M, N), they can be continuously parameterized by μ and e. To differentiate it with the orbit families in the CRTBP, the term *orbit group* rather than *orbit family* is used. According to the periodicity criterion, ME-Halo orbits perpendicularly cross the x–z plane twice and these two crosses can occur whether primaries are at periapsis or apoapsis. Categories first introduced by Campagnola et al. (2008) is summarized below and explained more rigorously.

If M is odd, after half a period, two crosses occur at two sides of ME-Halo, so the orbit is different whether it starts at $f_0 = 0$ or $f_0 = \pi$, which indicates the primaries are at their periapsis or apoapsis. Let the orbit starts from the left side (in the x–y projection) of the ME-Halo orbit, define *Periapsis Group* to start at $f_0 = 0$ and *Apoapsis Group* to start at $f_0 = \pi$. If the orbit starts from the right side, it will coincide with one of the two groups depending on that N is even or odd. In Fig. 4 the Earth–Moon L_1 periapsis group and apoapsis group ME-Halos with $M5N2$ are depicted as examples, with the Earth–Moon eccentricity adopted as 0.0554. The most obvious difference between them is that the relative position where the perpendicular cross occurs, marked by red small circle. As shown in the y–z projection, for periapsis ME-Halo it occurs at the outer circle and for apoapsis at the inner circle.

If M is even, two crosses occur at the same side of ME-Halo orbit and the orbit can be different whether the cross is on the left or right side of the orbit. Let the orbit starts at $f_0 = 0$, define *Left Group* to start from the left side and *Right Group* from the right side. If the orbit starts at $f_0 = \pi$, it will coincide with one of the two groups as well. In Fig. 5 the Earth–Moon L_2 left and right group ME-Halo orbits with $M2N1$ are depicted as examples.

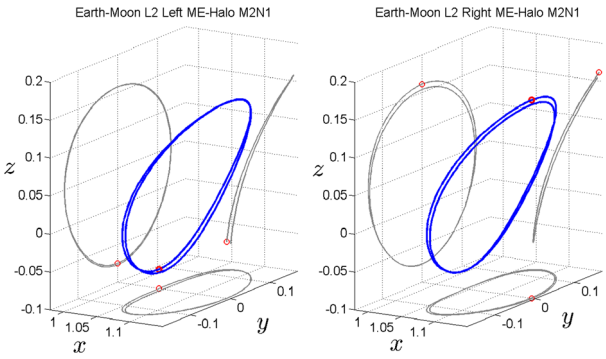

Fig. 5 Earth–Moon L_2 *Left* (*left plot*) and *Right* (*right plot*) ME-Halo orbit with $M2N1$ in the pulsating synodic frame

The most obvious difference is the position of the bifurcation of the orbit. For Left Group it is at the top and for Right Group the bottom.

Moreover, there are north and south halo orbits in the CRTBP, so each group defined here possesses a north and a south branch that are symmetric with respect to the x–y plane. In this paper only the north branch is chosen as the study object.

2.5 Monodromy matrix and stability indices

The monodromy matrix of a periodic orbit is defined as the state transition matrix (STM) over one period. In the ERTBP, the STM $\boldsymbol{\Phi}(f, f_0)$ satisfies

$$\boldsymbol{\Phi}'(f, f_0) = \boldsymbol{A}_E(X, f)\boldsymbol{\Phi}(f, f_0), \quad \boldsymbol{\Phi}(f, f_0) = \boldsymbol{I}_6,$$

where $\boldsymbol{A}_E(\boldsymbol{X}, f)$ is the Jacobian of Eq. (5)

$$\boldsymbol{A}_E(\boldsymbol{X}, f) = \begin{bmatrix} 0 & \boldsymbol{I}_3 \\ \boldsymbol{H}_C & \boldsymbol{K}_C \end{bmatrix}_{(\boldsymbol{X}, f)}, \quad \boldsymbol{H}_E = \begin{bmatrix} \omega_{xx} & \omega_{xy} & \omega_{xz} \\ \omega_{yx} & \omega_{yy} & \omega_{yz} \\ \omega_{zx} & \omega_{zy} & \omega_{zz} \end{bmatrix}_{(\boldsymbol{X}, f)},$$

$$\boldsymbol{K}_E = \begin{bmatrix} 0 & 2 & 0 \\ -2 & 0 & 0 \\ 0 & 0 & 0 \end{bmatrix}_{(\boldsymbol{X}, f)}. \tag{21}$$

The subscripts of ω indicate partial differentials with respect to corresponding coordinates. The independent variable is true anomaly f here. The periodic orbit in a periodic system is stable if and only if all eigenvalues of the monodromy matrix $\boldsymbol{\Psi}(f) = \boldsymbol{\Phi}(f + T_E, f)$ have modules smaller than one (Bittanti and Colaneri 2009). Since eigenvalues of $\boldsymbol{\Psi}(f)$ are invariant along the periodic orbit, they can be calculated at any convenient point. In this paper, the monodromy matrix $\boldsymbol{\Psi}(f_0)$ of ME-Halo is obtained by propagating Eq. (5) together with Eq. (21) from f_0 to $f_0 + T_E$. For Periapsis, Left and Right Group ME-Halo orbits $f_0 = 0$ is adopted and for Apoapsis Group $f_0 = \pi$ is adopted. In the situation where the ME-Halo orbit is given by multiple segments, the STM matrix $\boldsymbol{\Phi}$ for each segment can be calculated separately and then multiplied up as

$$\boldsymbol{\Psi}(f_0) = \boldsymbol{\Phi}(f_0 + T_E, f_0) = \boldsymbol{\Phi}(f_0 + T_E, f_{n-1}) \ldots \boldsymbol{\Phi}(f_2, f_1) \cdot \boldsymbol{\Phi}(f_1, f_0). \tag{22}$$

If directly integrate for one period T_E from the very first initial condition, the initial deviation will be magnified exponentially, and the deviation it caused to the monodromy matrix can affect its eigen-structure. But if $\boldsymbol{\Psi}$ is calculated separately according to Eq. (22), the numerical

process appears more steady. It is hard to tell how these deviations effect the final eigenvalues, since $\boldsymbol{\Phi}(f_{i+1}, f_i)$ has no direct relationship with the final $\boldsymbol{\Psi}$. This trick given by Eq. (22) can solve the problem of numerical accuracy in a sense because the orbit in segments are with the same accuracy. However, as M and N grow larger, the total integration time increases, and this causes the largest eigenvalue become larger exponentially and the smallest become smaller. Very quickly they will differ more than 20 orders, and this will cause the $\boldsymbol{\Psi}$ intrinsically not able to be numerically obtained will enough accuracy. So this is a crucial restriction that the ME-Halo orbits with $N = 2$ are studied, even though we could generate ME-Halo orbits with a larger N. The authors suppose a more profound insight into the stability of these orbit requires more advanced mathematic methods dealing with the nonlinearity.

In the CRTPB, the monodromy matrix of a halo orbit usually has a pair of eigenvalues equal to one because the system is Hamiltonian and autonomous. But in the ERTBP this is not the truth because of the appearance of eccentricity e and the non-autonomous features (Broucke 1969). The eigenvalues of ME-Halo orbits in the ERTBP come in reciprocal pairs as (Campagnola 2010)

$$\lambda_1, \frac{1}{\lambda_1}, \lambda_2, \frac{1}{\lambda_2}, \lambda_3, \frac{1}{\lambda_3}$$

Following the notation of Broucke (1969) and Sarris (1989), the stability index of ME-Halo is defined as

$$k_i = \lambda_i + 1/\lambda_i, \quad i = 1, 2, 3$$

This gives a simple criterion in most situations that the orbit is unstable if any $k_i > 2$. The only exception is that if there are two pairs of reciprocal complex eigenvalues which are conjugate but not on the unit circle, they will give complex k_i. If the other pair of eigenvalue is on the unit circle, then the criterion fails. The definition of stability indices is slightly modified to be include this rare situation as

$$k_i = \begin{cases} 2 \cdot \max\left(|\lambda_i|, |1/\lambda_i|\right), & \text{if } \lambda_i \text{ is complex and } |\lambda_i| \neq 1, \\ \lambda_i + 1/\lambda_1, & \text{others.} \end{cases} \tag{23}$$

With this new definition, two pairs of conjugate complex eigenvalues not on the unit circle will give the same index larger than 2, so that the criterion is sufficient and necessary. This definition is consistent with classic definitions. There is discontinuities when eigenvalues bifurcates away from the unit circle, as will be discussed in Sect. 3.2, however, this cannot be easily evaded without change classic definitions about stability indices. It is worth to note that Broucke (1969) also observed the complex instability in the planar ERTBP, where there are two pairs of eigenvalues conjugate with respect to the unit circle.

3 Numerical results and discussions

In this paper, the L_1 ME-Halo orbit with $M5N2$ is chosen as objects, where $M5N2$ means $M = 5$ and $N = 2$. And there are two groups of orbit as discussed in Sect. 2.4. Beside of stability properties, the authors are as well seeking for practical applications of the ME-Halo orbit. Halo orbits with this set of (M, N) in the Earth–Moon system are adequately far away from the Moon to be practically useful, as illustrated in Fig. 2. Another consideration of this choice is that their periods can be numerically handled.

The variation of the stability of ME-Halo orbits is studied with respect to parameters μ and e. The parameter space analyzed here is spanned by $\mu \in [0.001, 0.020]$ and $e \in [0, 0.210]$

with constant step sizes $\delta\mu = 0.001$ and $\delta e = 0.001$. The orbits are firstly continued along μ with $e = 0$. Then they are continued along e for each μ using parallel computing. The integrator ode45 in Matlab is used with an absolute tolerance of 3×10^{-14} (normalized unit, same unites for others) and a relative tolerance of 3×10^{-14}. For the continuation, the nonlinear constraint tolerance is 1×10^{-10}, which is the upper boundary of all discontinues at the connection points between two segments. After obtain databases with thousands of ME-Halo orbits, the eigenvalues of monodromy matrices of each orbit are calculated by the multi-segment method in Sect. 2.5. Before integration, each orbit is refined to four segments, so that less deviations will be introduced by Eq. (22). The same tolerances are adopted during this procedure. Finally, the stability property is analyzed by stability indices, and sometimes directly by eigenvalues.

During the study, the mass ratio μ is observed to have a greater impact than eccentricity e. The ME-Halo orbit is needed to be broken into about 32 segments to accomplish one continuation by $\delta\mu$, but only eight segments by δe. Averagely, for one step continuation by $\delta\mu$ it takes about 170 s, and by δe about 60 s. The data is serially collected on a 64-bit PC with a CPU of 3.2 GHz maximally. This can be explained by the fact that in the Legendre polynomial expansion of Eq. (5) (Lei et al. 2013), μ arises since the first-order terms, but e arises only from the second-order terms.

3.1 Periapsis group of ME-Halo orbits

In this subsection, the stability of the L_1 Periapsis Group of ME-Halo orbits with $M5N2$ is investigated. The characteristic curves of the orbits in this group are given by their initial conditions in the subspace (x_0, z_0, y_0') in the six-dimensional phase space, since they perpendicularly start from the x–z plane, i.e., $y_0 = x_0' = z_0' = 0$ for $\boldsymbol{X}_0 = [x_0, y_0, z_0, x_0', y_0', z_0']^{\mathrm{T}}$. The characteristic curves are depicted in Fig. 6. Each curve corresponds to a specific mass ratio μ as annotated. The curve is colored by the eccentricity of the primaries, growing from zero (green vertex) to the continuation end or 0.21 (red vertex). The curves show two clearly different trends. At $\hat{\mu} = 0.012$ the curve is the shortest, and it separates the two trends. For $\mu > \hat{\mu}$, y_0' of the curves keep descending, but for smaller $\mu < \hat{\mu}$ the curves bend in the

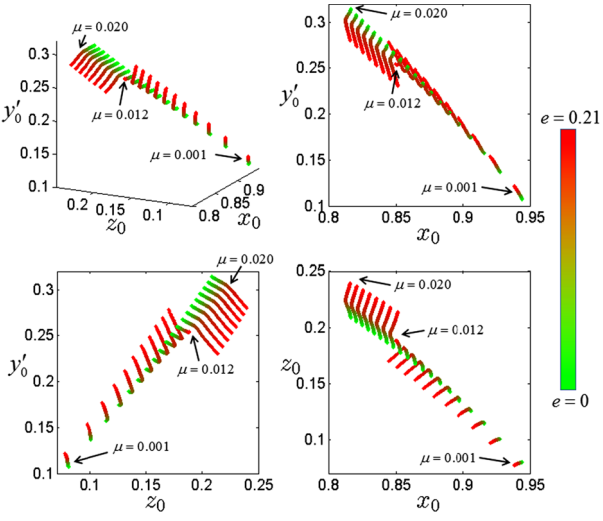

Fig. 6 Characteristic curves of the L_1 Periapsis Group ME-Halo with $M5N2$ in the subspace (x_0, z_0, y_0'). Curves corresponding to fixed mass ratio μ show different trends with e. The curves with larger μ keep descending. The curves with smaller μ bend in the *middle* and start to increase, and they have different length because the continuation algorithm fails to converge at $\hat{e}(\mu)$

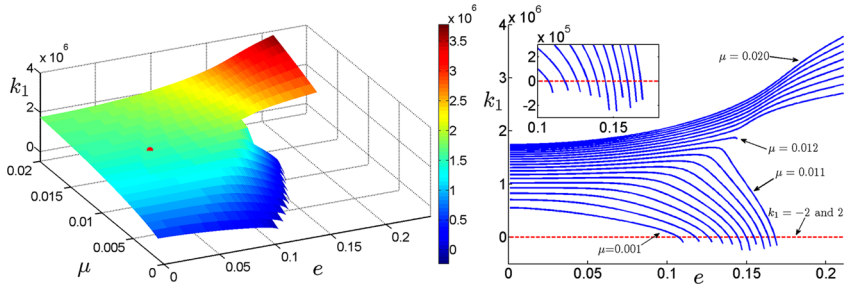

Fig. 7 Stability index surface $k_1(\mu, e)$ (*left plot*) and curves $k_1(e)_\mu$ (*right plot*) of the L_1 Periapsis Group ME-Halo with $M5N2$. The *small dot* (*red*) on the surface stands for the parameters of the Earth–Moon system (the same in following figures). For smaller μ, it becomes very negative though not demonstrated in this figure

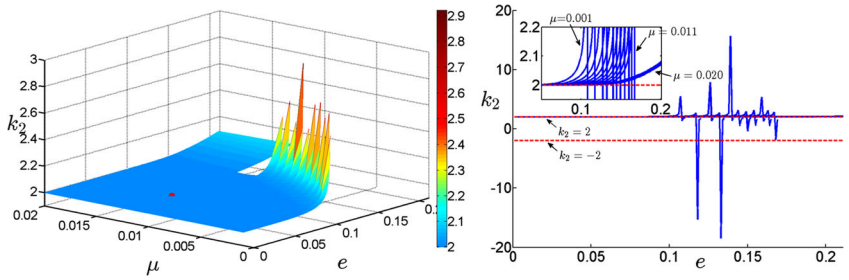

Fig. 8 Stability index surface $k_2(\mu, e)$ (*left plot*) and curves $k_2(e)_\mu$ (*right plot*) of the L_1 Periapsis Group ME-Halo with $M5N2$. For smaller μ, it becomes very negative before $\hat{e}(\mu)$, though not demonstrated in this figure

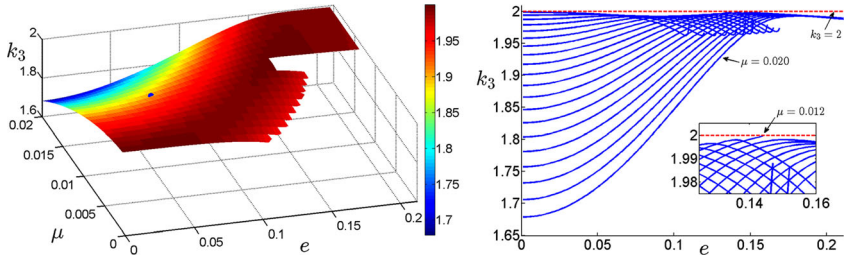

Fig. 9 Stability index surface $k_3(\mu, e)$ (*left plot*) and curves $k_3(e)_\mu$ (*right plot*)of the L_1 Periapsis Group ME-Halo with $M5N2$. It is always below $k_3 = 2$

middle, y_0' of the curves start to go upward and stop at a critical eccentricity $\hat{e}(\mu) < 0.21$. The continuation algorithm fails to converge at $\hat{e}(\mu)$. The algorithm could converge with a smaller step, but then it needs to further reduce the step until below the integration accuracy. Besides, all successful continuations can converge with any accuracy no higher than the integration accuracy, but any continuation covering $\hat{e}(\mu)$ cannot converge to the tolerance. The ME-Halo orbits later displayed in Fig. 10 do not show any obvious mechanisms that might cause this problem, like a close flyby, so it can be inferred that either there is a bifurcation or the characteristic curve is not monotonic with respect to the continuation parameter, which causes the failure of continuation using our algorithm. Moreover, the stability analysis later shows that the eigenvalues of the ME-Halo orbit near $\hat{e}(\mu)$ have great changes.

The stability index surfaces $k_i(\mu, e)$ (i $= 1, 2, 3$) of this group of orbits are depicted separately in the left plots of Figs. 7, 8 and 9 separately. The small dots (red or blue) on

the surfaces stand for the parameters of the Earth–Moon system. There is a clear and big great gap at $\hat{\mu} = 0.012$ in all figures, and the trends on two sides of the gap are different. When $\mu < \hat{\mu}$, k_1 decreases, k_2 increases and k_3 increases with e, but when $\mu > \hat{\mu}$, k_1, k_2 and k_3 all increase with e (the parameters and subscripts of k_i are dropt for simplicity if no ambiguity). These surfaces have very complex details, as will be revealed by separated curves $k_i(e)_\mu$ depicted in following three figures (the subscript μ indicates that the mass ratio is fixed). In the right plot of Fig. 7, the curves $k_1(e)_{\mu<\hat{\mu}}$ drop to below $k_1 = -2$ at $\hat{e}(\mu)$, the curve $k_1(e)_{\mu=\hat{\mu}}$ stops earlier than its adjacent curves, and the curves $k_1(e)_{\mu>\hat{\mu}}$ increase steadily. In the enlarged drawing, it is more clear that $k_1(e)_{\mu<\hat{\mu}}$ falls to below -2. There seems to be an infinite discontinuous point at the end of the continuation because the end of $k_1(e)_{\mu<\hat{\mu}}$ is nearly vertical. In this circumstance, a tiny incensement of e will cause very large variation of k_1, which could explains the reduction of the step required by the algorithm and its final failures. In the right plot of Fig. 8, the curves $k_2(e)_\mu$ appear all horizontal, but there are abrupt variations looking like computational errors. In the enlarged drawing, it is clear that the curves $k_2(e)_{\mu\leq\hat{\mu}}$ rise rapidly and fall down at last, but the curves $k_2(e)_{\mu>\hat{\mu}}$ grow slowly and steady. The seeming errors are caused by plotting when trying to connect one large positive point and one small negative point. In fact, $k_2(e)_{\mu<\hat{\mu}}$ suddenly drops to below -2, rises to the stable region for the next step and then the algorithm fails, as will be shown more delicately later. In the right plot of Fig. 9, the curves $k_3(e)_{\mu<\hat{\mu}}$ drop and stop after sudden rises, and the curves $k_3(e)_{\mu>\hat{\mu}}$ smoothly rise to nearly 2 and decrease slowly. It is interesting that the enlarged drawing reveals that the curve $k_3(e)_{\hat{\mu}}$ stops almost exactly at $k_3 = 2$, which means that λ_3 almost equals one. The word almost is used here because it needs very high accuracy and complex calculations to locate an eigenvalue on the unit circle. However, there is a clear trend that the curve between these two different kinds would interact with the boundary.

To further analyze the differences between these two trends, two branches of orbits in the Periapsis Group with constant mass ratio μ, $0.009 < \hat{\mu}$ and $0.015 > \hat{\mu}$ separately, are chosen as representatives in the following study. They are referred to as the *lighter branch* and the *heavier branch* for convenience, because μ is the normalized mass of the second primary. The comparison starts from their orbit shapes. In Figs. 10 and 11, lighter and heavier branches of ME-Halo orbits with various e are depicted separately in pulsating and non-pulsating synodic frames, and separately in x–y and x–z projections. The orbits in the pulsating synodic frame (upper red) is displaced along positive vertical axis for clarity, but those in the non-pulsating frame (lower blue) are depicted as they are. Firstly, discussions are made about the plots in

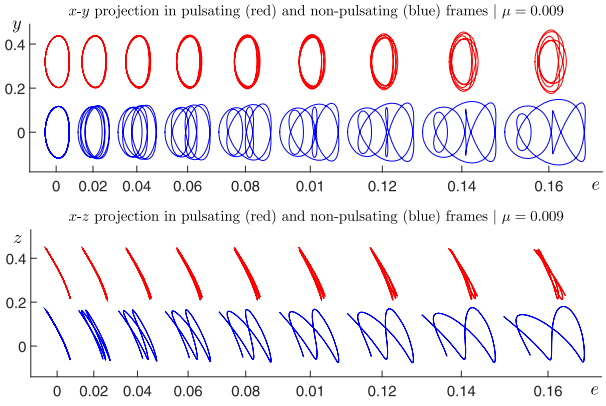

Fig. 10 Lighter branches of Periapsis Group ME-Halo orbits with $\mu = 0.009$, depicted in pulsating (*upper red*) and non-pulsating (*lower blue*) frame separately

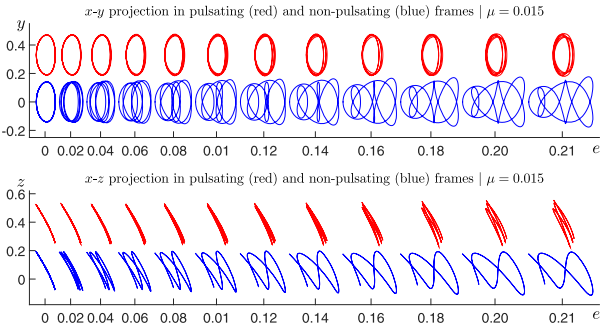

Fig. 11 Heavier branches of Periapsis Group ME-Halo orbits with $\mu = 0.015$, depicted in pulsating (*upper red*) and non-pulsating (*lower blue*) frame separately

Table 1 Eigenvalues of orbits of the lighter branch illustrated in Fig. 10

e	λ_1	$1/\lambda_1$	λ_2	$1/\lambda_2$	λ_3	$1/\lambda_3$
0	1.3112e+06	7.6258e−07	1.0002	0.9998	0.9587 + 0.2843i	0.9587 − 0.2843i
0.02	1.3169e+06	7.5937e−07	1.0008	0.9993	0.9607 + 0.2777i	0.9607 − 0.2777i
0.04	1.3338e+06	7.4995e−07	1.0043	0.9957	0.9662 + 0.2577i	0.9662 − 0.2577i
0.06	1.3615e+06	7.3453e−07	1.0119	0.9882	0.9745 + 0.2245i	0.9745 − 0.2245i
0.08	1.3978e+06	7.1573e−07	1.0250	0.9756	0.9840 + 0.1782i	0.9840 − 0.1782i
0.10	1.4324e+06	6.9841e−07	1.0452	0.9567	0.9927 + 0.1206i	0.9927 − 0.1206i
0.12	1.3515e+06	7.3979e−07	1.0778	0.9278	0.9976 + 0.0696i	0.9976 − 0.0696i
0.14	8.0075e+05	1.2486e−06	1.2073	0.8283	0.9929 + 0.1190i	0.9929 − 0.1190i
0.16	−2.1676e+05	−4.6133e−06	0.8705 + 0.4922i	0.8705 − 0.4922i	0.9896 + 0.1440i	0.9896 − 0.1440i

the pulsating frame (upper red). In the x–y projection, the orbits of the lighter branch shrinks more than that of the heavier branch. In the x–z projection, the multiple revolutions of the heavier branch separate each other further without crosses as e grows, but that of the lighter branches shows a clear cross after $e = 0.12$, where the right revolutions lean to the left. Secondly, the plots in the non-pulsating frame (lower blue) are compared. The orbits until $e = 0.12$ appears all the same, but after this they are different. In the x–y projection, the two left loops of the lighter branch detach into an outer loop and an inner small loop, but those of the heavier branch always keep contact with each other. The middle loop unfolds differently as well. For the lighter branch the left side of the middle loop is more vertical than the right side, but for the heavier branch they appear symmetric. In the x–z projection, the lighter branch stretches to upper direction as e increases, while the heavier branch stretches to lower direction.

The eigenvalues of the monodromy matrix of the orbits depicted in Figs. 10 and 11 are listed in Tables 1 and 2. The first orbits with $e = 0$ in both branches are the halo orbits revolving $M = 5$ revolutions in the corresponding CRTBP systems, so their true value of λ_2 (or $1/\lambda_2$) should be one. But in both tables, the values are not identically one, which are 1.0002 and $1.0000 + 0.0001$i separately. This is caused by numerical errors during long-time integrations, and the data suggest that there are at least four significant digits. In Table 1, the lighter branch shows a big change from $e = 0.12$ to 0.16, where λ_1 starts to decrease and finally falls below zero and λ_2 becomes complex at the same time.

The analysis of the stability indices above, as well as their different orbit shapes, reveal that lighter branches have a great change just before the end of the continuation along e. To

Table 2 Eigenvalues of the monodromy matrix of the orbits illustrated in Fig. 11

e	λ_1	$1/\lambda_1$	λ_2	$1/\lambda_2$	λ_3	$1/\lambda_3$
0	1.5966e+06	6.2662e−07	1.0000 + 0.0001i	1.0000 − 0.0001i	0.9021 + 0.4316i	0.9021 − 0.4316i
0.02	1.6061e+06	6.2247e−07	1.0006	0.9994	0.9052 + 0.4250i	0.9052 − 0.4250i
0.04	1.6351e+06	6.1197e−07	1.0035	0.9965	0.9142 + 0.4053i	0.9142 − 0.4053i
0.06	1.6845e+06	5.9376e−07	1.0098	0.9903	0.9282 + 0.3721i	0.9282 − 0.3721i
0.08	1.7563e+06	5.6919e−07	1.0202	0.9802	0.9457 + 0.3250i	0.9457 − 0.3250i
0.10	1.8536e+06	5.3984e−07	1.0359	0.9654	0.9647 + 0.2635i	0.9647 − 0.2635i
0.12	1.9825e+06	5.0427e−07	1.0594	0.9439	0.9824 + 0.1870i	0.9824 − 0.1870i
0.14	2.1633e+06	4.6247e−07	1.1003	0.9089	0.9948 + 0.1014i	0.9948 − 0.1014i
0.16	2.4712e+06	4.0464e−07	1.1624	0.8603	0.9982 + 0.0601i	0.9982 − 0.0601i
0.18	2.7552e+06	3.6307e−07	1.2374	0.8082	0.9971 + 0.0764i	0.9971 − 0.0764i
0.20	2.9533e+06	3.3824e−07	1.3246	0.7549	0.9954 + 0.0962i	0.9954 − 0.0962i
0.21	3.0388e+06	3.2940e−07	1.3749	0.7273	0.9944 + 0.1059i	0.9944 − 0.1059i

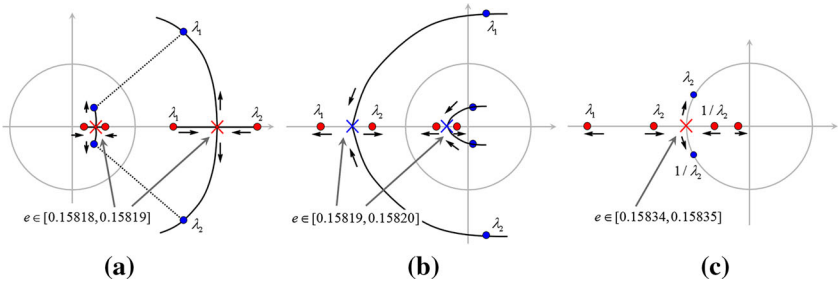

Fig. 12 Illustrations of the three collision and bifurcations of λ_1 and λ_2 of the lighter branch in Table 1. Their reciprocals are illustrated but not annotated. The annotated intervals contain the eccentricities at which they occur

figure out the variation in this eccentricity interval, a detailed analysis with continuation steps as least as $\delta e = 2.5 \times 10^{-6}$ is carried out. The variation is found to be complicate, and the eigenvalues collide and bifurcate three times as shown in Fig. 12. The collisions occur in the intervals annotated in the figure. It needs to be noticed that in the interval between subplot a) and b) the ME-Halo orbit has all eigenvalues complex but two pairs of them conjugate with respect to the unit circle, and in the interval between subplot b) and c) the ME-Halo orbit has two pairs of negative eigenvalues. However, the ME-Halos in Fig. 10 before and after this process do not show much differences. We suggest this phenomenon is caused by the interaction between μ and e, which cannot likely be explained by numerical studies. As a comparison, in Table 2, the heavier branch shows less complexity, where λ_1 keeps increasing and grows quicker than λ_2. So there is no collision during the whole interval from 0 to 0.21. This again reflects that when μ is larger, the effect of the eccentricity is relatively smaller.

Figure 13 demonstrates various ME-Halo orbits on the x–y plane with the critical orbit with $\hat{\mu} = 0.012$ and $\hat{e}(\hat{\mu}) = 0.143$ in the center of the figure. Parameters of each plot are annotated below it. The center row shows the orbits with the same eccentricity 0.143 but different mass ratio. The first two are empty because the continuation fails ahead of 0.143. The upper row shows the orbits at the continuation end of respective μ (for $\mu = 0.012$ it

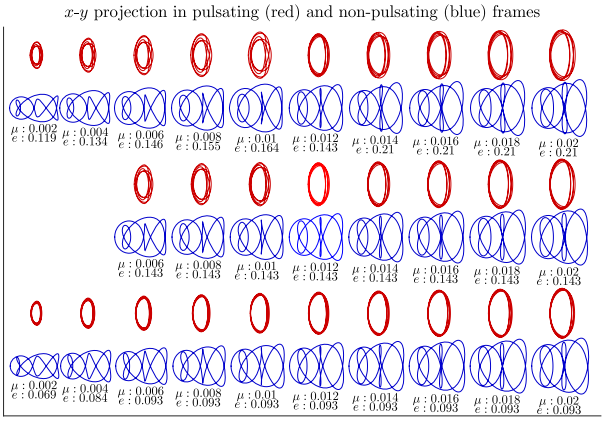

Fig. 13 Variation of Periapsis Group ME-Halo orbits around the critical orbit with $\mu = 0.012$ and $e = 0.143$

is identical to the center row). The bottom row shows the orbits with a $\delta e = 0.05$ ahead of orbit just above it, which means for the first two ahead of the continuation end, and for others ahead of 0.143. There are some clear differences among these orbits. In the non-pulsating plots (blue), for small μ the loops in the middle shrink greatly compared with their beginnings (in the sense of eccentricity), but for larger μ these loops always keep relatively the same size and even tend to stretch vertically. Reflected in the pulsating plots (red), for small μ the orbits disperse gradually and the inner regions shrink, but for larger μ the orbits appear more regular.

3.2 Apoapsis group of ME-Halo orbits

In this subsection, the stability of the L_1 Apoapsis Group of ME-Halo orbits with $M5N2$ is investigated. The characteristic curves of the orbits in this group are also given by their initial conditions in the subspace $(x_0, z_0, \dot{y}_0)$ in the phase space, which are illustrated in Fig. 14. Each curve in the plots corresponds to a specific mass ratio μ as annotated. The curve is colored by the eccentricity of the primaries, growing from zero (green vertex) to 0.21 (red vertex). The curves show clearly different trends as well. For $\mu \geq 0.011$ y_0' of the curves keep descending, but for smaller $\mu \leq 0.010$ the curves bend in the middle and y_0' of the curves start to go upward. What differs from that of the Periapsis Group is that all curves extend to $e = 0.210$ successfully. Like what for the Periapsis Group, there tends to exist a specific $\hat{\mu} \in (0.010, 0.011)$ separating these two trends as well. But it was not directly detected by the discrete grids.

In Fig. 15, the stability index surface $k_1(e, \mu)$ is smooth but the trend of the surface has a gap around $\hat{\mu}$ $(0.010 < \hat{\mu} < 0.011)$. The stability index curve plot on the left shows that the curves $k_1(e)_{\mu<\hat{\mu}}$ fall down to as small as 500, but turn upward after a critical eccentricity $\hat{e}$. This is a significant difference from the previous Periapsis Group, which might guarantees the successful continuation to $e = 0.210$. The curves $k_2(e)_\mu$ and $k_3(e)_\mu$ are depicted together in Fig. 16. The curves with $\mu < \hat{\mu}$ and $\mu > \hat{\mu}$ are separated since they have different magnitudes and clearly different trends. It should be noticed that all three enlarged plots shows that k_2 and k_3 coincide with each other for specific intervals, and the lower figure shows discontinuities which are results of the modified definition of stability indices. At these changing points, λ_2 and λ_3 become complex eigenvalues but not on the unit circle. It is also worth to note that in the enlarged plot of the upper figure, the curves shows again two different trends, for

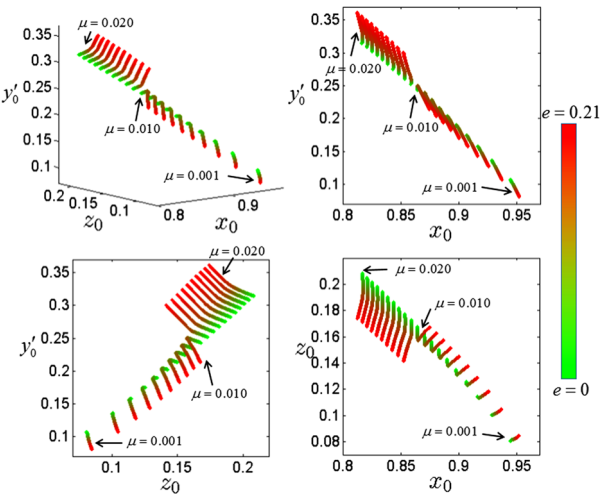

Fig. 14 Characteristic curves of the L_1 Apoapsis Group of ME-Halo orbits with $M5N2$ in the subspace (x_0, z_0, y_0') and their projections. Curves corresponding to fixed mass ratio μ show different trends as e grows larger. The curves with larger μ keep descending. The curves with smaller μ bend in the middle and start to increase. All the curves extend to $e = 0.21$ successfully

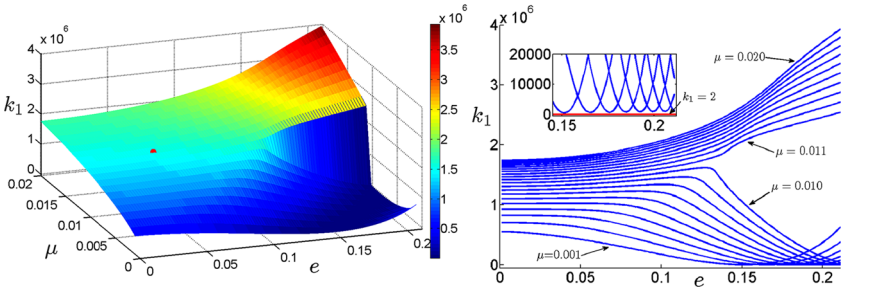

Fig. 15 Stability index surface $k_1(\mu, e)$ and various curves $k_1(e)_\mu$ of the L_1 Apoapsis Group ME-Halo with $M5N2$. They are always above the stability boundary $k_1 = 2$, which means λ_1 and $1/\lambda_1$ are always real and positive. The surface and curves behave differently before and after the gap around some separator $\hat{\mu} \in (0.010, 0.011)$

example $k_{2,3}(e)_{\mu=0.010}$ has two arches but most others have only one. So totally there are three kinds of stability evolutions in this Apoapsis Group. In the similar way, three branches of ME-Halo orbits are chosen as representatives to study. They are the *lighter branch* with $\mu = 0.004$, the *medium branch* with $\mu = 0.009$, and the *heavier branch* with $\mu = 0.015$. The variation of the shape of the orbits of these three branches are demonstrated in Figs. 17, 18 and 19. In the x–y projections of all three figures, for the orbits in the non-pulsating frame, the inner loops of the lighter and medium branches shrink and separate from the outer loops as e increases, but that of the heavier branch remain contact with the outer loop; for that in the pulsating frame, the orbits all shrink to the center but less severe for the heavier branch. Another obvious difference is that in the x–z projections, the orbits in Figs. 17 and 18 stretch more severely in the right half of the projection after $e = 0.15$, just where their stability indices k_2 and k_3 become very negative in Fig. 16, but the orbits in Fig. 19 appear to stretch more uniformly.

The eigenvalues of the ME-Halo orbits of three branches are listed in Tables 3, 4 and 5, from which the variations can be viewed directly. It needs to be notice that the first lines of each table correspond to the ideal halo orbits in the CRTBP. And as mentioned before, the numerical error of λ_2 in the table, which should be one ideally, indicates there are at least

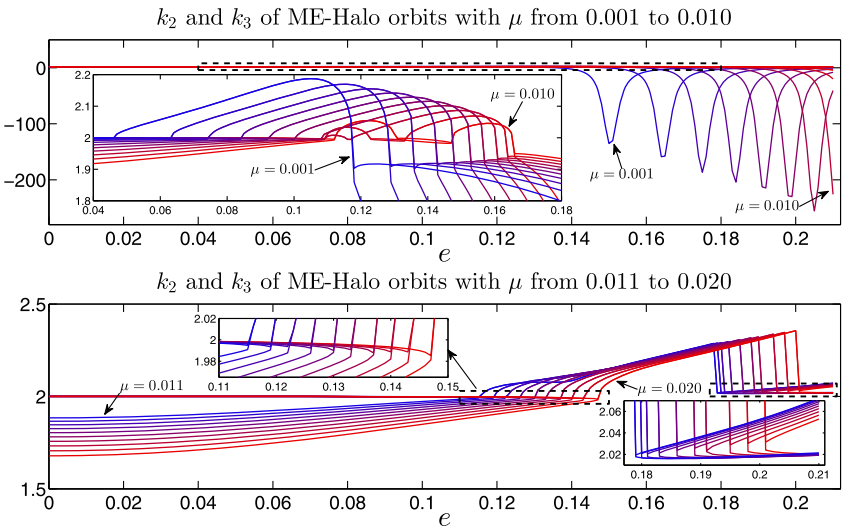

Fig. 16 Stability index curves of $k_2(e)_\mu$ and $k_3(e)_\mu$ of the L_1 Apoapsis Group of ME-Halo orbits. The *upper plot* and the enlarged drawing there show two different trends of the lighter and medium branches. The *lower plot* shows all similar trends of the heavier branch, which has two abrupt change points as shown in two enlarged drawings

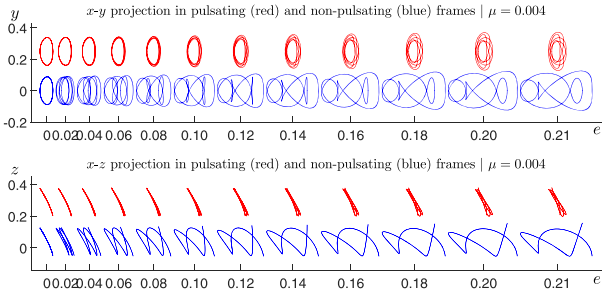

Fig. 17 Lighter branch of L_1 Apoapsis ME-Halo orbits with $\mu = 0.004$, depicted in pulsating (*upper red*) and non-pulsating (*lower blue*) frames separately

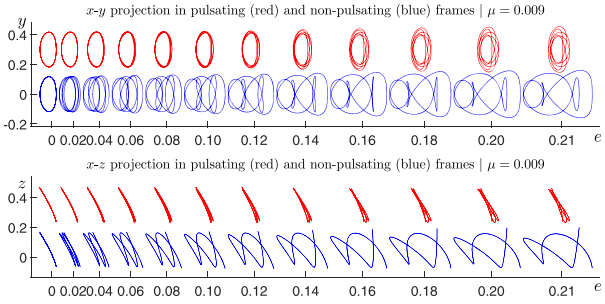

Fig. 18 Medium branch of L_1 Apoapsis ME-Halo orbits with $\mu = 0.009$, depicted in pulsating (*upper red*) and non-pulsating (*lower blue*) frames separately

four significant digits. For all branches, λ_1 is always large positive real values. λ_2 and λ_3 show great differences among three branches. The lighter and medium branches has complex eigenvalue variations as reflected in Fig. 16. Combined with the sudden rises in Fig. 16, it can be observed that the lighter branch has only one interval from about $e = 0.10$ to $e = 0.14$ where λ_2 and λ_3 are with modules larger than 1, but the medium branch has two intervals

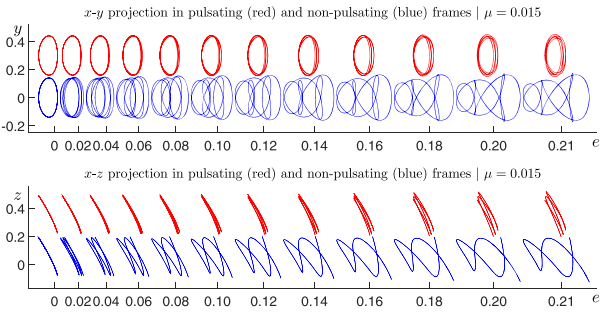

Fig. 19 Heavier branch of L_1 Apoapsis ME-Halo orbits with $\mu = 0.015$, depicted in pulsating (*upper red*) and non-pulsating (*lower blue*) frames separately

Table 3 Eigenvalues of orbits of the lighter branch with $\mu = 0.004$ illustrated in Fig. 17

e	λ_1	$1/\lambda_1$	λ_2	$1/\lambda_2$	λ_3	$1/\lambda_3$
0	9.3110e+05	1.0740e−06	1.0004	0.9996	0.9021 + 0.4316i	0.9021 − 0.4316i
0.02	9.3063e+05	1.0746e−06	0.9905 + 0.1378i	0.9905 − 0.1378i	0.9052 + 0.4250i	0.9052 − 0.4250i
0.04	9.2647e+05	1.0793e−06	1.0000 + 0.0060i	1.0000 − 0.0060i	0.9142 + 0.4053i	0.9142 − 0.4053i
0.06	9.0444e+05	1.1056e−06	0.9952 + 0.0977i	0.9952 − 0.0977i	0.9282 + 0.3721i	0.9282 − 0.3721i
0.08	8.1800e+05	1.2225e−06	0.9967 + 0.0808i	0.9967 − 0.0808i	0.9457 + 0.3250i	0.9457 − 0.3250i
0.10	6.4486e+05	1.5507e−06	1.0320 + 0.1017i	0.9597 − 0.0946i	0.9647 + 0.2635i	0.9647 − 0.2635i
0.12	4.3834e+05	2.2812e−06	1.0502 + 0.1743i	0.9267 − 0.1538i	0.9824 + 0.1870i	0.9824 − 0.1870i
0.14	2.3927e+05	4.1794e−06	1.0019 + 0.2994i	0.9163 − 0.2738i	0.9948 + 0.1014i	0.9948 − 0.1014i
0.16	8.1398e+04	1.2285e−05	0.5867 + 0.8098i	0.5867 − 0.8098i	0.9982 + 0.0601i	0.9982 − 0.0601i
0.18	2.8907e+03	3.4593e−04	−46.5318	−0.0215	0.9971 + 0.0764i	0.9971 − 0.0764i
0.20	5.0494e+04	1.9805e−05	−2.6794	−0.3732	0.9954 + 0.0962i	0.9954 − 0.0962i
0.21	1.4006e+05	7.1400e−06	−0.1870 + 0.9824i	−0.1870 − 0.9824i	0.9944 + 0.1059i	0.9944 − 0.1059i

Table 4 Eigenvalues of orbits of the medium branch with $\mu = 0.009$ illustrated in Fig. 18

e	λ_1	$1/\lambda_1$	λ_2	$1/\lambda_2$	λ_3	$1/\lambda_3$
0	1.3112e+06	7.6272e−07	1.0000 + 0.0001i	1.0000 − 0.0001i	0.9587 + 0.2843i	0.9587 − 0.2843i
0.02	1.3169e+06	7.5949e−07	1.0000 + 0.0008i	1.0000 − 0.0008i	0.9607 + 0.2777i	0.9607 − 0.2777i
0.04	1.3339e+06	7.4968e−07	1.0000 + 0.0043i	1.0000 − 0.0043i	0.9662 + 0.2577i	0.9662 − 0.2577i
0.06	1.3623e+06	7.3434e−07	0.9745 + 0.2245i	0.9745 − 0.2245i	0.9999 + 0.0119i	0.9999 − 0.0119i
0.08	1.4018e+06	7.1325e−07	0.9997 + 0.0248i	0.9997 − 0.0248i	0.9841 + 0.1778i	0.9841 − 0.1778i
0.10	1.4487e+06	6.9018e−07	0.9990 + 0.0457i	0.9990 − 0.0457i	0.9931 + 0.1169i	0.9931 − 0.1169i
0.12	1.4488e+06	6.9014e−07	1.0102 + 0.0656i	0.9858 − 0.0640i	1.0102 − 0.0656i	0.9858 + 0.0640i
0.14	1.0349e+06	9.6637e−07	1.0121 + 0.1266i	0.9728 − 0.1217i	1.0121 − 0.1266i	0.9728 + 0.1217i
0.16	6.2201e+05	1.6077e−06	1.0015 + 0.2330i	0.9472 − 0.2204i	1.0015 − 0.2330i	0.9472 + 0.2204i
0.18	2.8905e+05	3.4596e−06	0.8384 + 0.5451i	0.8384 − 0.5451i	0.9623 + 0.2718i	0.9623 − 0.2718i
0.20	6.6894e+04	1.4949e−05	−0.4359 + 0.9000i	−0.4359 − 0.9000i	0.9421 + 0.3354i	0.9421 − 0.3354i
0.21	1.1938e+04	8.3769e−05	−19.7985	−0.0505	0.9288 + 0.3705i	0.9288 − 0.3705i

Table 5 Eigenvalues of orbits of the heavier branch with $\mu = 0.015$ illustrated in Fig. 19

e	λ_1	$1/\lambda_1$	λ_2	$1/\lambda_2$	λ_3	$1/\lambda_3$
0	1.5966e+06	6.2636e−07	1.0002	0.9998	0.9021 + 0.4316i	0.9021 − 0.4316i
0.02	1.6061e+06	6.2266e−07	0.9052 + 0.4250i	0.9052 − 0.4250i	1.0000 + 0.0006i	1.0000 − 0.0006i
0.04	1.6351e+06	6.1147e−07	0.9142 + 0.4053i	0.9142 − 0.4053i	1.0000 + 0.0035i	1.0000 − 0.0035i
0.06	1.6851e+06	5.9339e−07	0.9282 + 0.3721i	0.9282 − 0.3721i	1.0000 + 0.0097i	1.0000 − 0.0097i
0.08	1.7590e+06	5.6862e−07	0.9457 + 0.3250i	0.9457 − 0.3250i	0.9998 + 0.0200i	0.9998 − 0.0200i
0.10	1.8623e+06	5.3682e−07	0.9648 + 0.2630i	0.9648 − 0.2630i	0.9994 + 0.0353i	0.9994 − 0.0353i
0.12	2.0062e+06	4.9841e−07	0.9834 + 0.1814i	0.9834 − 0.1814i	0.9982 + 0.0600i	0.9982 − 0.0600i
0.14	2.2197e+06	4.5037e−07	1.0508 + 0.0908i	0.9446 − 0.0816i	1.0508 − 0.0908i	0.9446 + 0.0816i
0.16	2.5436e+06	3.9332e−07	1.0935 + 0.0561i	0.9121 − 0.0468i	1.0935 − 0.0561i	0.9121 + 0.0468i
0.18	2.8381e+06	3.5188e−07	1.1411 + 0.0264i	0.8759 − 0.0203i	1.1411 − 0.0264i	0.8759 + 0.0203i
0.20	3.0812e+06	3.2454e−07	1.2449	0.8033	1.1417	0.8759
0.21	3.1997e+06	3.1249e−07	1.2950	0.7722	1.1489	0.8704

around $e = 0.12$ and $e = 0.14 \sim 0.16$. Within these intervals, the ME-Halo orbits has two pairs of eigenvalues out of but conjugate with respect to the unit circle. Later on, they both change to have a pair of negative eigenvalues as revealed in both Fig. 16 and the tables. The heavier branches has three pairs of eigenvalues, and they all show increasing trends as revealed in Fig. 16, which indicates that the ME-Halo orbit is very unstable with these parameters, all states near it in the phase space will eventually leaving it along the three-dimensional unstable manifold quickly. Among the changes between these different distributions, there exist the collision and bifurcations of the eigenvalues on the complex plane. This comparison among three branches shows that the eccentricity has more complicate effects when the mass ratio is relatively small.

3.3 Earth–Moon ME-Halo orbits

The Earth–Moon system has a relatively large eccentricity and revolves faster than usual solar planetary systems, so it could be more helpful to design deep space trajectories in a more real model, for example the ERTBP which has considered the orbital eccentricity. The mass ratio of the Earth–Moon system is adopted as 0.0122 and the eccentricity as 0.0554. Compared with a halo orbit in the CRTBP, an ME-Halo orbit can capture more features in the ephemeris model, such as the pulsating motion along the x-axis caused by the elliptical motion of the Moon. The stability of ME-Halo orbits Earth–Moon system is demonstrated in stability index surfaces in Sects. 3.1 and 3.2. For clarity, they are summarized here. The L_1 Periapsis ME-Halo orbit has two pairs of real eigenvalues, $(\lambda_1, 1/\lambda_1)$ and $(\lambda_2, 1/\lambda_2)$, and a pair of complex unit eigenvalues $(\lambda_3, 1/\lambda_3)$. λ_1 is very large, about 1.5427×10^6, but $\lambda_2 = 1.0086$ is only slightly bigger than 1. The L_1 Apoapsis orbit has only one pair of real eigenvalue $(\lambda_1, 1/\lambda_1)$, and two pairs of complex unit eigenvalues $(\lambda_2, 1/\lambda_2)$ and $(\lambda_3, 1/\lambda_3)$, where $\lambda_2 = 1.5431 \times 10^6$ is larger than that of the Periapsis. The shapes of these two orbits are illustrated in Fig. 4 in Sect. 2.4. Although the ME-Halo orbit will not be precisely periodic in the ephemeris model, it can be seen that the appearance of eccentricity has dynamically changed the stability properties. Generally speaking, the orbits in the ERTBP appear more unstable than that in the CRTBP.

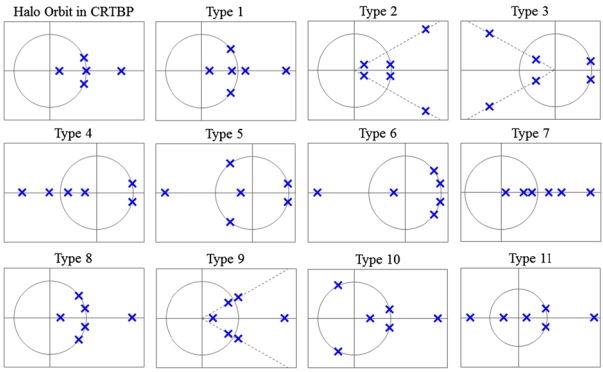

Fig. 20 Summary of eigenvalue distributions on the complex plane of the ME-Halo orbits investigated in this paper

3.4 Collisions and bifurcations

Campagnola had observed that the stability of left and right ME-Halo orbits with $M2N1$ in the Earth–Moon system bifurcates at $e = 0$ (Campagnola et al. 2008; Campagnola 2010). In this paper, bifurcations and collisions of the eigenvalues of another two groups of ME-Halo orbit are observed. All types of eigenvalue distributions observed during the study are summarized in Fig. 20. The first plot shows that of the halo orbit in the CRTBP from which the continuation starts. It has a pair of eigenvalues equal to one. It can be observed in other plots of Fig. 20 that an ME-Halo orbit can have as many as three pairs of real eigenvalues. The evolution of the eigenvalues of different branches of orbits are summarized below:

- L_1 Periapsis Group with $M5N2$, lighter branch: Type 1 → Type 2 → Type 3 → Type 4 → Type 5 → Type 6.
- L_1 Periapsis Group with $M5N2$, heavier branch: Type 1.
- L_1 Apoapsis Group with $M5N2$, lighter branch: Type 8 → Type 9 → Type 8 → Type 10 → Type 11 → Type 10.
- L_1 Apoapsis Group with $M5N2$, medium branch: Type 8 → Type 9 → Type 8 → Type 9 → Type 8 → Type 10 → Type 11.
- L_1 Apoapsis Group with $M5N2$, heavier branch: Type 8 → Type 9 → Type 7.

Generally the heavier branches show less complexity. On the other hand, the eccentricity e usually has relatively greater effects on the stability property of ME-Halo orbits when μ is small. This can be preliminarily explained by the Legendre polynomial expansion of the equations of motion (Lei et al. 2013). The eccentricity e only arises from the second order terms, it will have less effect, but when it is comparable with effect of the mass ratio μ, for example if e is 10 times of μ it might show more severe effect. However, a quantified result can hardly be drawn from the present numerical study.

4 Concluding remarks

In this paper the authors systematically studied the stability properties of two groups of ME-Halo orbits generated by a multi-segment optimization method. ME-Halo orbits are strictly periodic orbits in the nonautonomous ERTBP model which revolves M circles around the libration point region in one period when primaries revolve N circles. The orbits are generated by continuing from a halo orbit with commeasurable period in the CRTBP with

mass ratio μ to the ERTBP with the same μ and a nonzero eccentricity e. The multi-segment optimization method is proposed to accomplish the continuation because the traditional differential correction method diverges. The monodromy matrix is used to numerically study the stability of ME-Halo orbits, which is generated also in a multi-segment way consist with the generation of ME-Halo orbits. The L_1 Periapsis and Apoapsis Group of ME-Halo orbits are generated in the parameter region spanned by $\mu \in [0.001, 0.020]$ and $e \in [0, 0.21]$. Different evolutions of the eigenvalues with e are observed. Totally eleven distribution types of eigenvalues are observed in this study. Different collision and bifurcations of eigenvalues are analyzed as well.

According to the numerical exploration, the Periapsis Group has two different branches, and the apoapsis group has three different branches. The emergence of the eccentricity in the system introduces great complexity. An ME-Halo orbit can have as much as three pairs of real eigenvalues, one or two pairs of negative eigenvalues, and two pairs of complex eigenvalues out of the unit circle. Also, eigenvalues of particular orbits are negative. These are all very different from halo orbits in the CRTBP. Moreover, the eccentricity e shows more significant effect on the stability evolution when the mass ratio μ is small. In the Periapsis Group, a continuation barrier arises for small mass ratio, which seems to be caused by the change of eigenvalues from positive to negative but still needs more analytical studies in the future. Since the ME-Halo orbit captures more natural dynamics, its specific stability features can provide potentially practical applications. These properties will be helpful especially in fast systems like the Earth–Moon system or very eccentric systems like the Sun–Mercury system.

Acknowledgments The research presented in this paper was supported by the State Key Program of National Natural Science of China (Grant No. 11432001). The authors would like to thank all editors and the anonymous reviewers for all their hard work. The reviewers not only gave critical comments on the paper which greatly improves the quality of this paper, but also generously shared their knowledge, insights and suggestions with us, which are very helpful for our future research.

References

Antoniadou, K.I., Voyatzis, G.: 2/1 Resonant periodic orbits in three dimensional planetary systems. Celest. Mech. Dyn. Astron. **115**(2), 161–184 (2013). doi:10.1007/s10569-012-9457-4

Barden, B., Howell, K.C., Lo, M.: Application of dynamical systems theory to trajectory design for a libration point mission. 268–281 (1996). doi:10.2514/6.1996-3602

Belbruno, E.A., Gidea, M., Topputo, F.: Geometry of weak stability boundaries. Qual. Theory Dyn. Syst. (2012). doi:10.1007/s12346-012-0069-x

Bittanti, S., Colaneri, P.: Periodic Systems, vol. 36. Communications and Control Engineering. Springer, London (2009)

Broucke, R.A.: Stability of periodic orbits in the elliptic, restricted three-body problem. AIAA J. **7**(6), 1003–1009 (1969). doi:10.2514/3.5267

Campagnola, S.: New Techniques in Astrodynamics for Moon Systems Exploration. Ph.D. Dissertation, University of Southern California (2010)

Campagnola, S., Lo, M.W., Newton, P.: Subregions of motion and elliptic halo orbits in the elliptic restricted three-body problem. In: 18th AAS/AIAA Spaceflight Mechanics Meeting, Galveston (2008)

Farquhar, R.W., Kamel, A.A.: Quasi-periodic orbits about the translunar libration point. Celest. Mech. **7**(4), 458–473 (1973). doi:10.1007/BF01227511

Gomez, G., Koon, W.S., Lo, M.W., Marsden, J.E., Masdemont, J.J., Ross, S.D.: Connecting orbits and invariant manifolds in the spatial restricted three-body problem. Nonlinearity **17**(5), 1571–1606 (2004). doi:10.1088/0951-7715/17/5/002

Gurfil, P., Kasdin, N.J.: Niching genetic algorithms-based characterization of geocentric orbits in the 3D elliptic restricted three-body problem. Comput. Methods Appl. Mech. Eng. **191**(49–50), 5683–5706 (2002). doi:10.1016/S0045-7825(02)00481-4

Gurfil, P., Meltzer, D.: Semi-analytical method for calculating the elliptic restricted three-body problem monodromy matrix. J. Guid. Control Dyn. **30**(1), 266–271 (2007). doi:10.2514/1.22871
Heppenheimer, T.A.: Out-of-plane motion about libration points: nonlinearity and eccentricity effects. Celest. Mech. **7**(2), 177–194 (1973). doi:10.1007/BF01229946
Hiday, L.A., Howell, K.C.: Transfers between libration-point orbits in the elliptic restricted problem. Celest. Mech. Dyn. Astron. **58**(4), 317–337 (1994). doi:10.1007/BF00692008
Hou, X.Y., Liu, L.: On motions around the collinear libration points in the elliptic restricted three-body problem. Mon. Not. R. Astron. Soc. **415**(4), 3552–3560 (2011). doi:10.1111/j.1365-2966.2011.18970.x
Howell, K.C., Pernicka, H.J.: Numerical determination of Lissajous trajectories in the restricted three-body problem. Celest. Mech. **41**(1–4), 107–124 (1987). doi:10.1007/BF01238756
Hyeraci, N., Topputo, F.: Method to design ballistic capture in the elliptic restricted three-body problem. J. Guid. Control. Dyn. **33**(6), 1814–1823 (2010). doi:10.2514/1.49263
Hyeraci, N., Topputo, F.: The role of true anomaly in ballistic capture. Celest. Mech. Dyn. Astron. **116**(2), 175–193 (2013). doi:10.1007/s10569-013-9481-z
Ichtiaroglou, S.: Elliptic Hill's problem—the continuation of periodic orbits. Astron. Astrophys. **92**, 139–141 (1980)
Ichtiaroglou, S., Michalodimitrakis, M.: Three-body problem—the existence of families of three-dimensional periodic orbits which bifurcate from planar periodic orbits. Astron. Astrophys. **81**, 30–32 (1980)
Koon, W.S., Lo, M.W., Marsden, J.E., Ross, S.D.: Shoot the moon. In: Spaceflight Mechanics 2000. Advances in Astronautical Sciences. No. 105. American Astronautical Society, pp. 1017–1030. San Diego (2000)
Koon, W.S., Lo, M.W., Marsden, J.E., Ross, S.D.: Dynamical Systems, The Three-Body Problem and Space Mission Design. Marsden Books (2011)
Lei, H., Xu, B., Hou, X., Sun, Y.: High-order solutions of invariant manifolds associated with libration point orbits in the elliptic restricted three-body system. Celest. Mech. Dyn. Astron. **117**(4), 349–384 (2013). doi:10.1007/s10569-013-9515-6
Mahajan, B.: Libration point orbits near small bodies in the elliptic restricted three-body problem. Masters Theses. Paper 7200 (2013). http://scholarsmine.mst.edu/masters_theses/7200
Mahajan, B., Pernicka, H.J.: Halo orbits near small bodies in the elliptic restricted problem. 1–9 (2012). doi:10.2514/6.2012-4876
Martin, C., Conway, B.A., Ibáñez, P.: Optimal Low-Thrust Trajectories to the Interior Earth-Moon Lagrange Point. In: Space Manifold Dynamics, pp. 161–184. New York, NY: Springer (2010)
Meyer, K.R., Hall, G.R., Offin, D.: Introduction to Hamiltonian dynamical systems and the N-body problem. In: Antman S.S., Marsden J.E., Sirovich L. (eds.) Applied Mathematical Sciences, vol. 90, 2nd edn. Springer, New York (2009)
Moulton, F.R.: Periodic Orbits. Carnegie Institution of Washington, Washington (1920)
Parker, J.S., Anderson, R.L.: Low-energy lunar trajectory design, 1st edn. In: JPL Deep-Space Communications and Navigation Series. Wiley (2014)
Pernicka, H.J.: The numerical determination of nominal libration point trajectories and development of a station-keeping strategy. Purdue University (1990)
Qi, Y., Xu, S.: Lunar capture in the planar restricted three-body problem. Celest. Mech. Dyn. Astron. **120**(4), 401–422 (2014). doi:10.1007/s10569-014-9582-3
Qi, Y., Xu, S., Qi, R.: Gravitational lunar capture based on bicircular model in restricted four body problem. Celest. Mech. Dyn. Astron. **120**(1), 1–17 (2014a). doi:10.1007/s10569-014-9554-7
Qi, Y., Xu, S., Qi, R.: Study of the gravitational capture at mercury in the elliptic restricted three-body problem. In: Proceedings 24th International Symposium on Space Flight Dynamics—24th ISSFD, 2014.05.06 (2014b)
Richardson, D.L.: Analytic construction of periodic orbits about the collinear points. Celest. Mech. **22**(3), 241–253 (1980). doi:10.1007/BF01229511
Russell, R.P.: Survey of spacecraft trajectory design in strongly perturbed environments. J. Guid. Control Dyn. **35**(3), 705–720 (2012). doi:10.2514/1.56813
Sarris, E.: Families of symmetric-periodic orbits in the elliptic three-dimensional restricted three-body problem. Astrophys. Space Sci. **162**(1), 107–122 (1989). doi:10.1007/BF00653348
Szebehely, V.G.: Theory of Orbits—The Restricted Problem of Three Bodies. Academic Press, New York (1967)
Tarragó, P.I.: Study and assessment of low-energy Earth–Moon transfer trajectories. Université de Liège (2007)
Wiggins, S.: Introduction to Applied Nonlinear Dynamical Systems and Chaos, 2nd edn. Springer, New York (2003). http://www.springer.com/us/book/9780387001777#aboutBook